nature communications

Article

https://doi.org/10.1038/s41467-026-69692-7

Mach-Zehnder atom interferometry with non-interacting trapped Bose-Einstein condensates

Received: 14 May 2025

Accepted: 30 January 2026

Published online: 11 April 2026

Check for updates

T. Petrucciani[1,7], A. Santoni[2,3,7], C. Mazzinghi[1,3], D. Trypogeorgos[4], F. S. Cataliotti[1,3], M. Inguscio[1,3,5], G. Modugno[3,5], A. Smerzi[1,3,6], L. Pezzè[1,3,6] ✉ & M. Fattori[1,3,5] ✉

The coherent manipulation of a quantum wave is at the core of quantum sensing. For instance, atom interferometers require splitting and recombination processes to map the accumulated phase shift into a measurable population signal. Although Bose-Einstein condensates (BECs) are the archetype of coherent matter waves, their manipulation in double-well potentials has been limited by the strong interparticle collisions dominating over the tunneling energy. Here, we overcome this problem by using BECs with tunable interactions trapped in an innovative array of double-well potentials and exploiting quantum tunneling to realize coherent beam splitting. We operate several Mach-Zehnder interferometers in parallel, canceling common-mode potential instabilities by a differential analysis, thus demonstrating a trapped-atom gradiometer. Furthermore, by applying a spin-echo protocol, we suppress additional decoherence sources and approach unprecedented coherence times of one second. Our interferometer will find applications in precision measurements of forces with a sub-micron spatial resolution and in linear manipulation of quantum entangled states for sensing with sub-shot-noise sensitivity.

Bose-Einstein Condensates (BECs) of ultracold atomic gases[1,2] are recognized as powerful tools for both fundamental research[3,4] and emerging quantum technologies[5–7]. Often regarded as the matter-wave analog of lasers[8,9], BECs hold particular promise in the domain of high precision measurements[10]. Thanks to their remarkably low momentum spread[11], they are currently exploited in free-falling atom interferometers within drop towers[12–18] and earth-orbiting research laboratories[19]. Trapped atom interferometers[20–23] that exploit the unique properties of BECs promise to bring measurements of gravity, inertial forces and electromagnetic fields into a new realm. The large spatial coherence of a quantum degenerate gas enables splitting a BEC in two interferometric modes with large separation, allowing for high-sensitive measurements. Moreover, the quantum-limited size of a BEC provides high spatial resolution for sensing applications[10].

Among the several interferometric schemes with trapped BEC[24–28], much effort has been devoted to the realization of double-well systems[29–32] where the two spatial modes are separated by a potential barrier and coupled by tunneling[33–36]. These interferometers could enable force measurements with high spatial resolution in compact setups. However, collisions between atoms in high-density samples have caused dephasing of the interferometric signal[37,38] and obstructed the realization of coherent beam splitters. Previous valuable attempts to overcome these issues[36,39] have been limited by the short coherence times and a reduction of the interference contrast.

[1]National Institute of Optics, National Research Council (CNR-INO), Florence, Italy. [2]University of Naples Federico II, Naples, Italy. [3]European Laboratory for Nonlinear Spectroscopy (LENS), Sesto Fiorentino, Italy. [4]Institute of Nanotechnology, National Research Council (CNR-Nanotec), Lecce, Italy. [5]Department of Physics and Astronomy, University of Florence, Sesto Fiorentino, Italy. [6]QSTAR, Florence, Italy. [7]These authors contributed equally: T. Petrucciani, A. Santoni. ✉e-mail: luca.pezze@ino.cnr.it; fattori@lens.unifi.it

Additionally, interatomic collisions prevent the linear rotations of the Bloch vector associated to the many-particle quantum entangled states[40], which are necessary for the operation of the interferometer below the shot-noise limit[41]. A possible solution involves tuning the collisional scattering length to zero via magnetic Feshbach resonances – as already employed to suppress interaction-induced dephasing in Bloch oscillation[42,43]. However, non-interacting gases make the interferometer extremely sensitive to imperfections in the trapping potential. This occurs because even small energy mismatches between the wells directly translate into uncontrolled phase shifts, in the absence of the mean-field self-compensation whereby interactions generate a population imbalance that reduces the effective bias[44,45]. Therefore, despite early optimistic expectations, atom interferometry based on BECs confined in a double-well trap has yet to fully realize its potential in the field of precision metrology.

In this work we overcome current roadblocks and demonstrate the operation of a full Mach-Zehnder Interferometer (MZI) with non-interacting BECs trapped in two spatially separated modes. The key ingredient is an innovative potential[46] made of an array of Double-Well (DW) traps where several interferometers operate simultaneously. In this way, residual instabilities of the trap, that could mask the coherence of a single sensor, are common mode and can be canceled using a differential analysis. Therefore, our system also realizes the first trapped atom gradiometer reported in the literature, extending the range of applicability of a technique already exploited in free falling atom interferometers[47]. Each MZI (see the scheme in Fig. 1) consists of a beam splitter, an interrogation time, and a final beam splitter that maps the accumulated relative phase into a population imbalance. The beam splitters operate in the linear regime with near-unit contrast by canceling inter-particle interactions via a magnetic Feshbach resonance and by tuning the height of the barrier separating each DW - changing the tunneling energy. By implementing a spin-echo protocol[48], we suppress residual technical noise and extend the interferometer's coherence time to ~1 s, nearly two orders of magnitude longer than previously reported values[36,39]. Our results unlock the full potential of trapped atom interferometry with BECs, establishing it as a powerful and promising platform for quantum-enhanced technologies.

Results

The experimental system consists of a BEC of ^{39}K atoms manipulated by an innovative array of DWs[46], where interactions are tuned to zero using a broad magnetic Feshbach resonance[49,50]. During the final part of the evaporation stage, two collinear optical lattices aligned along the horizontal x direction are switched on adiabatically. Their wavelengths $\lambda_1 \simeq 1013$ nm and $\lambda_2 \simeq 1064$ nm create a Beat-Note superlattice (BNSL)[51] with a spacing equal to $\frac{1}{2}\frac{\lambda_1\lambda_2}{\lambda_2-\lambda_1} \sim 10\,\mu$m. In this way, several independent BECs can be loaded in the minima of the potential, Fig. 1a. By using a third optical lattice superimposed to the others, and with wavelength $\lambda_3 \simeq 1120$ nm, we create an additional BNSL with spatial periodicity $d = \frac{1}{2}\frac{\lambda_3\lambda_1}{\lambda_3-\lambda_1} \sim 5\,\mu$m. By raising this optical potential in $t_{BS_1} = 10$ ms in the center of each BEC, we form an array of DWs (see Supplemental Material) and realize the first beam splitter of each MZI, see Fig. 1b. This operation is followed by an interrogation time T, see Fig. 1c. An external homogeneous force provides a linear potential energy that affects each interferometer with an equal energy mismatch ε between the two wells. A spatial-dependent force realized in our experiment with an additional vertical dipole trap laser, instead, provides an additional non-common energy difference δ between the two modes of each MZI, see Fig. 1c. By performing a further beam splitter (Fig. 1d), we map the accumulated phase onto a population difference (Fig. 1e).

The second beam-splitter exploits the Josephson dynamics in the linear regime (Rabi[35]) of non-interacting atoms tunneling through the central barrier of each DW. In order to optimize the beam-splitting sequence, we have performed a dedicated experiment. We start with a BEC initially loaded in the left well. We reduce the barrier height with a linear ramp and then raise it back again in 20 ms. This is done by acting on the third lattice depth leaving unchanged the first two. The minimum height of the barrier is adjusted in order to achieve a balanced beam splitter. The corresponding optimal sequence is shown in Fig. 2a. In Fig. 2b, we show the distribution of the population imbalance $z_j = (N_{L,j} - N_{R,j})/(N_{L,j} + N_{R,j})$ after the splitting sequence (see histogram in Fig. 2b). Here, $N_{R,j}$ and $N_{L,j}$ are the number of atoms in the right and left side of the j-th DW (j = 1, 2). Residual instabilities of the energy mismatch between the two modes prevents the achievement of shot-noise limited splitting (black line in Fig. 2b). Shorter sequences with larger tunneling energies could help to approach such limit, but they could cause unwanted excitations of the atoms to higher lying modes. The possibility to operate simultaneously two or more interferometers requires that the tunneling energy of neighboring DWs is equal. This is demonstrated in Fig. 2c, where we report the Rabi oscillations of z_j (for two neighboring DWs) as a function of tunneling time, at low barrier height. This measurement was performed by loading a BEC into the left site of an unbalanced double well. Over a period of 10 ms, the height of the central barrier was lowered while the energy offset between the two sites was compensated, thereby initiating a Rabi dynamics with an amplitude slightly smaller than the initial imbalance z ~ 1. The results show near-unity visibility of Rabi oscillations that would be prevented by particle-particle interactions[40].

In the following, we select two central DWs, each loaded with $N \approx 3000$ atoms. An external harmonic confinement of frequency $\omega/2\pi$, created by an additional vertical laser beam, causes a differential energy mismatch $\delta = m\omega^2 d^2$, where m is the atomic mass. This provides a phase difference between two interferometers equal to $\Delta\phi = \phi_1 - \phi_2 = \frac{\delta}{\hbar}T$, where ϕ_j is the interferometric phase acquired by the j-th interferometer. A plot of the two population imbalances, z_1 versus z_2, is shown in Fig. 3a. For two perfectly correlated interferometers with sinusoidal signals $z_j = V_j \sin(\phi_\varepsilon + \phi_j) + C_j$, where V_j are visibilities, C_j are oscillation offsets and ϕ_ε is a common-mode phase noise uniformly distributed between 0 and 2π, the measurements scatter along an ellipse whose eccentricity depends on the relative phase $\Delta\phi$[52–54],

$$\tilde{z}_1^2 + \tilde{z}_2^2 - 2\tilde{z}_1\tilde{z}_2\cos(\Delta\phi) - \sin^2(\Delta\phi) = 0, \quad (1)$$

where $\tilde{z}_j = (z_j - C_j)/V_j$. Values of V_j smaller than 1 are mainly due to unwanted excitations of the atoms to higher-lying states, finite temperature effects, and detection noise. Values of C_j different from 0 arise from unwanted energy mismatch between the two wells during the splitting sequences. Loss of correlations between the two interferometers, mainly due to the interactions and uncontrolled spatial inhomogeneities (see below), causes a spread of the experimental measurements out of the ellipse. We perform a multiparameter maximum likelihood analysis of the experimental data[55] and extract both the differential signal $\Delta\phi$ and the uncorrelated noise $\sigma_{\Delta\phi}$ (see "Methods"). To study $\Delta\phi$ as a function of T, we collect three sets of measurements of $\Delta\phi$ chosen in a $[-\pi, +\pi]$ interval around T = 20 ms, 45 ms and 85 ms (collected in three different days), see Fig. 3b. As expected, $\Delta\phi$ increases linearly with T, with a slope proportional to δ. The interaction is set on the zero crossing of a broad Feshbach resonance around 350 Gauss for atoms in the absolute ground state $|F = 1, m_F = 1\rangle$, where F is the hyperfine quantum number[43]. The interferometric determination of the external trapping frequency from such slopes is in agreement, within the error bars, with the value determined using atom sloshing in the external harmonic potential (see Fig. 3b and Supplemental Material).

To study the effect of interaction-induced dephasing, we fix T and analyze z_1 vs z_2 as a function of the atomic scattering length by tuning the magnetic field B. The corresponding values of $\sigma_{\Delta\phi}$ are shown in Fig. 4 (points). As expected, we observe a minimum around

https://doi.org/10.1038/s41467-026-69692-7

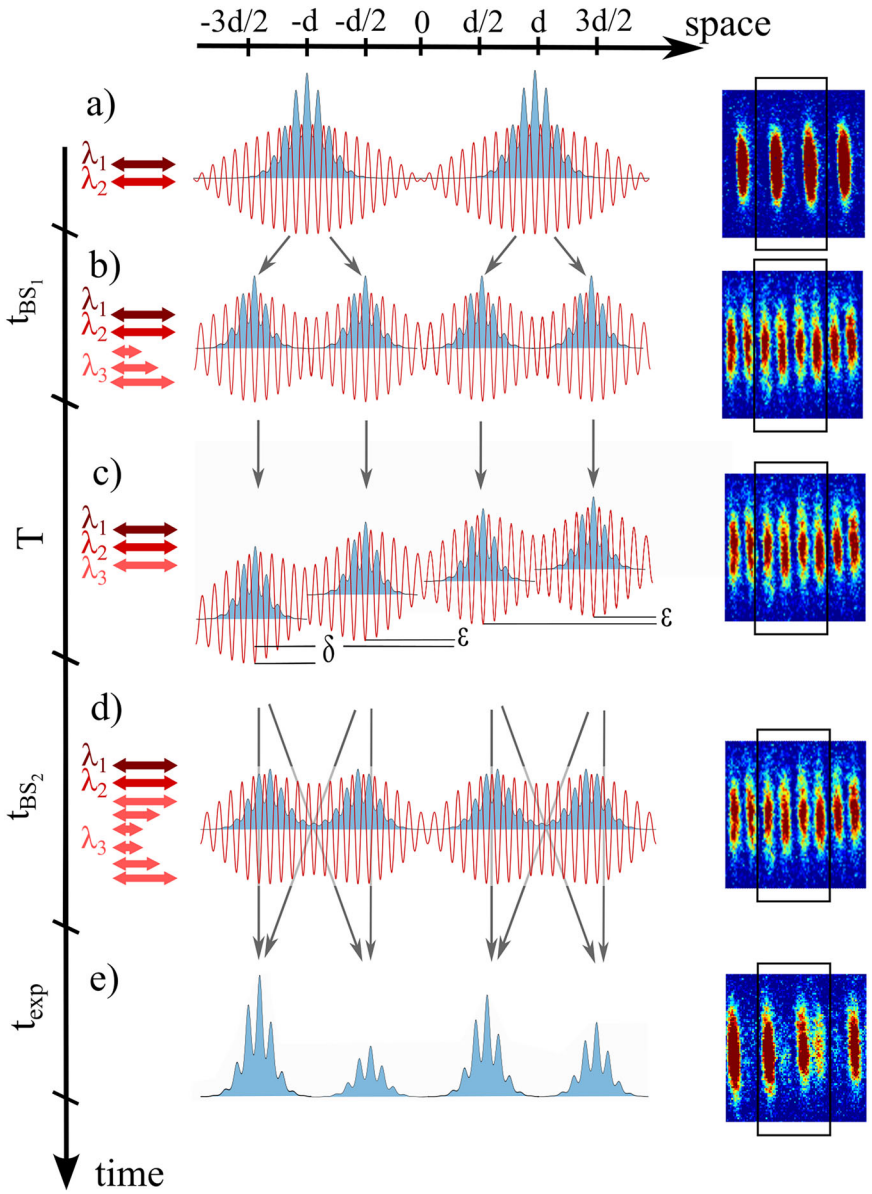

Fig. 1 | Gradiometer with trapped BEC Mach-Zehnder interferometers. The trapping potential (red line) is realized with two Beat-Note superlattices (BNSL)[51] formed by three retro-reflected lasers with wavelengths λ_1, λ_2 and λ_3: the intensity and manipulation of each lattice is schematically illustrated by the lateral arrows. Superposed to the trapping potential, we show 1D integrated profiles of the BEC density, while experimental absorption images are reported on the right. Different sections correspond to different stages of gradiometer operation implemented with non-interacting atoms. **a** *BEC array*. The two optical lattices λ_1 and λ_2 form a BNSL, with effective lattice sites separated by ~10 μm and loaded with independent BECs. The lattice depth is enough to suppress the tunneling between sites. **b** *Raising barrier beam-splitter*. The amplitude of the third lattice, with wavelength λ_3, is raised in a time t_{BS_1} splitting the clouds in two spatial modes separated by $d = 5$ μm. **c** *Phase shift*. During the interrogation time T, an external homogeneous force induces an equal energy shift ε in both DWs. Instead, a spatial dependent force introduces a differential energy shift δ. **d** *Tunneling linear beam-splitter*. The third lattice amplitude is first lowered and then raised again in a time t_{BS_2} to achieve a 50% tunneling probability between the two modes. **e** *Detection*. Final populations in the two modes of the interferometers are measured via standard absorption imaging after expansion of the atoms (t_{exp}) along the directions orthogonal to the lattices.

$B_{min} = 350.45(6)$ Gauss, in agreement with the previously reported value[56]. We compare the experimental results with the model including the effect of interactions, imperfect splitting and technical decoherence. We predict (see Supplemental Material) that the uncorrelated noise for an initial coherent state follows the behavior

$$\sigma^2_{\Delta\phi}(B) = \frac{2}{N}(1+\sigma^2_{BS}) + 2N(1+N\sigma^2_{BS})\left(\frac{\chi(B)T}{\hbar}\right)^2 + \sigma^2_{tech}. \quad (2)$$

Here, N is the number of atoms in each interferometer (assumed equal) and $\chi(B) = \chi_{el}(B) + \chi_{dd}$ is the sum of the elastic particle-particle (χ_{el}) and the dipolar (χ_{dd}) interaction within each well and σ_{tech} is the technical decoherence. We have $\chi(B) \propto (B - B_{min})$, where the interplay of the attractive χ_{dd} and the repulsive χ_{el} gives a specific value B_{min} such that $\chi = 0$. σ^2_{BS} quantifies the classical fluctuations of the mean value of z due to uncontrolled energy mismatch between the two DWs after the first beam splitter. Such fluctuations enhance the spread of the quantum state on the Bloch sphere due to non linear dynamics (see inset in Fig. 4) that cause a rotation of the Bloch vector with a speed that is proportional to the distance from the equator. The experimental data are well reproduced by Eq. (2).

https://doi.org/10.1038/s41467-026-69692-7

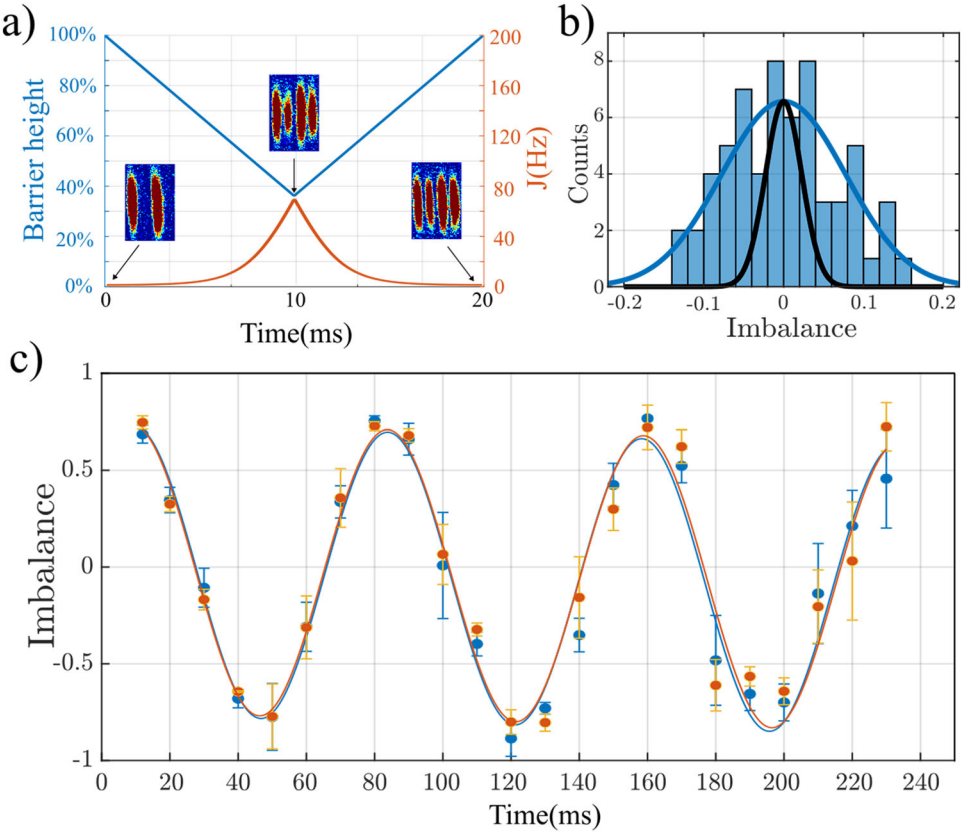

Fig. 2 | Tunneling atom beam-splitter. a Evolution of the DW parameters, barrier height (blue line) and tunneling energy (red line), that allows the BECs initially loaded in the left mode of each DW to tunnel to the right mode with 50% probability. **b** Histogram of the imbalance z for a single DW (see text) after the beam-splitting sequence. The blue line is the Gaussian fit of the data and the black line represents the projection noise. We obtain a noise of 0.078(19) from the width of the Gaussian fit, that is three times larger than the projection noise that is $\sqrt{2/N} \simeq 0.023$. **c** Synchronous Rabi oscillations show equal tunneling energy for two neighboring DWs. The points and the error bars show the mean and plus/minus one mean standard deviation on 3 measurements. The fitted Rabi frequencies are 13.4(3) Hz (blue line) and 13.3(3) Hz (orange line).

As shown by the previous analysis, near B_{min} interactions are minimized by the precise canceling of the scattering length and the primary source of noise remains σ_{tech}. Assuming that the technical decoherence is almost constant on the duration of the interferometer, but varying from shot to shot, it can be compensated by a spin-echo protocol. This consists of applying an additional π pulse at time $T/2$, midway through the interferometric sequence[57,58]. The spin echo is realized by a linear ramp of the barrier height, as in Fig. 2, but reaching a lower value (~30% of the initial height). Such sequence lasts a time long enough to allow the exchange of the occupation of the two clouds between the two spatial modes. Note that this sequence is achievable due to the unique capability of our apparatus to perform linear rotations around the x-axis of the Bloch sphere. In Fig. 5, we compare the measurements of $\sigma_{\Delta\phi}$ as a function of T for both the gradiometer and the spin-echo protocol with $B = B_{\mathrm{min}}$. Using the gradiometer scheme, we are able to measure a differential phase up to ≈200 ms (blue triangles). Instead, with the spin-echo protocol we reach a significant decoherence only after 400 ms (red circles). At this interrogation time, we further minimize the interaction-induced dephasing by finely tuning the Feshbach magnetic field. At the new optimum value B = 350.48(1) Gauss, using the spin-echo protocol, we extend the interrogation time up to T = 800 ms (yellow squares). The origin of the residual noise is under investigation. Multiple π pulses can be used to cancel the effect of differential phase drifts occurring on the timescale T. This will allow one to distinguish technical noise sources from fundamental limitations such as finite temperature or residual interparticle interactions.

Discussion

In conclusion, we report the realization of a Mach-Zehnder atom interferometer based on BECs trapped in DW potentials, where beam-splitting operations via tunneling through the separating barrier are enabled by the precise canceling of the interaction within each DW. Utilizing an innovative array of DWs, we successfully operate two interferometers simultaneously and demonstrate trapped atom gradiometry and spin-echo protocols with synchronous beam splitting pulses. Our multiparameter analysis of correlated data provides simultaneous access to both the differential signal and the dephasing – primarily attributed to residual particle-particle interactions– while effectively canceling common-mode phase noise. We report coherence times of almost 1 s, so far never achieved with BECs trapped in DW potentials[36,59].

Our work demonstrates a benchmark result in the coherent manipulation of a BEC between fully trapped spatial modes. The techniques we report open new paths for quantum sensing. The full control over the spatial mode of a trapped BEC makes our gradiometer ideal for high-precision force measurements with sub-micron spatial resolution[60–63]. Correlated analysis of several DW interferometers operating in parallel could be applied to the spatial reconstruction of non-uniform external potentials with common-mode noise rejection. Additionally, our system is an ideal tool to measure higher-order interaction terms, such as dipolar interactions[56,64,65] and three-body elastic collisions[66]. Interestingly, our platform offers the unique capability to tune the interactions, enabling the preparation of quantum-entangled states[6,67–69], and to cancel the scattering length during the interferometer operations.

https://doi.org/10.1038/s41467-026-69692-7

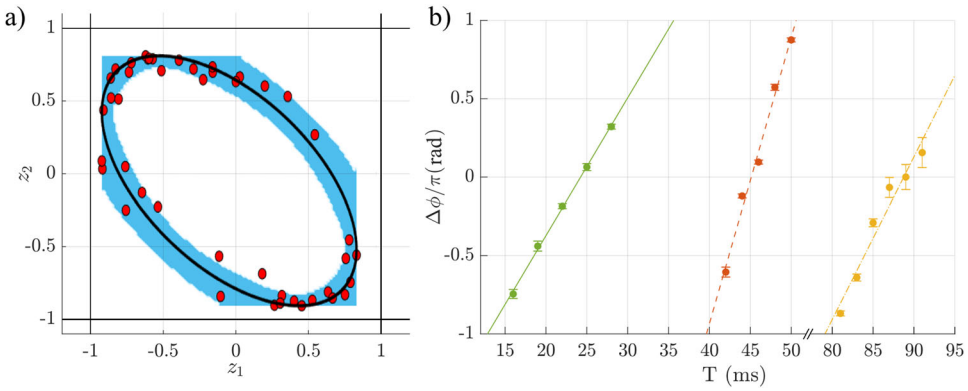

Fig. 3 | Gradiometric measurements. (**a**) Output population imbalances (red dots) of two neighboring DW interferometers. The black line represents the elliptical fit obtained using a maximum likelihood method (see text and "Methods"). The blue shaded region represents 90% confidence area of the fit. The estimated center of the ellipse is $C_1 = -0.0387(8)$, $C_2 = -0.066(5)$; the estimated visibilities are $V_1 = 0.89(2)$, $V_2 = 0.85(2)$. **b** $\Delta\phi$ as a function of T in three different time intervals around 20 ms, 45 ms and 85 ms. The three sets of measurements allow to estimate the trap frequency values from a linear fit: 17.9(6) Hz (solid line), 21.7(9) Hz (dashed line), 16.4(3) Hz (line-point). The error bars represent the standard deviation of the mean value computed with a bootstrap analysis (see "Methods"). Each point is obtained from the analysis of about 30 z_1 vs z_2 data. The three trap frequency values agree with the ones estimated from the oscillations of trapped BECs, that are 18.5(2) Hz, 20.5(4) Hz, 16.8(2) Hz. The different values are due daily variations of the vertical beam, used to create the harmonic potential.

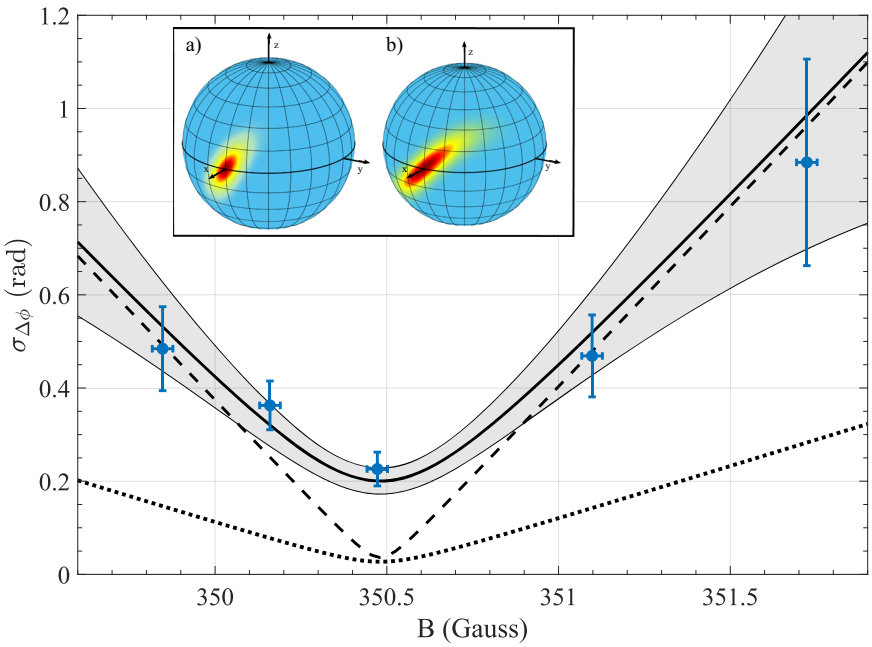

Fig. 4 | Interaction-induced dephasing. Uncorrelated noise $\sigma_{\Delta\phi}$ as a function of the magnetic field B tuning the particle-particle interaction scattering length. Dots are experimental results obtained at $T = 70$ ms. The vertical error bars are the standard deviation of the mean value computed with the Bootstrap analysis. The horizontal ones instead are the error on the determination of the magnetic field (see Supplemental Material). The dotted and dashed lines are Eq. (2) for $\sigma_{BS} = 0$ and $\sigma_{BS} = 0.07$ (obtained from an independent experimental characterization (see Supplemental Material)). The solid line is the result of numerical simulations that further include, see Eq. (2), an extra stochastic phase noise term $\sigma_{tech} = 0.15$ rad to fit the experimental data, (see Supplemental Material). The gray region show statistical mean squared fluctuations in the maximum likelihood fit due to the finite sample size (about 30 measurements). *Inset*: Wigner distribution of the time-evolved state represented on the generalized Bloch sphere. In (**a**), only quantum fluctuations on the first beam-splitter are considered and the dynamics is only due to one-axis-twisting[69], whereas in (**b**) further spread of the state is the result of extra fluctuations $\sigma_{BS} = 0.07$ after the first beam-splitter.

This opens the possibility to achieve sub-shot-noise sensitivities, also in the presence of strong environmental decoherence[70–72]. Finally, long coherence in a trapped BEC interferometer opens interesting perspectives in the development of compact and transportable devices for measurements of inertial forces and navigation applications[73,74].

Methods

Beat-note superlattice

The array of DWs is realized with three co-propagating lasers at wavelengths λ_1, λ_2 and λ_3 retroreflected on a common mirror to form three optical lattices[46]. The beam waist of the lasers is ≈500 μm and their powers of 300/380/250 mW provide optical lattice depths of 370/400/240 nK, respectively. Using a polarizing cube we can superimpose the three lattices with an additional dipole trap beam with a wavelength of 1064 nm and with a 12 μm waist. This laser beam provides a radial confinement of the trapped modes along the y and the vertical z direction of ≈180 Hz. Its weak longitudinal confinement along the x direction of ≈1 Hz does not prevent the simultaneous balancing of many DWs. In addition it is used in combination with another dipole trap beam

https://doi.org/10.1038/s41467-026-69692-7

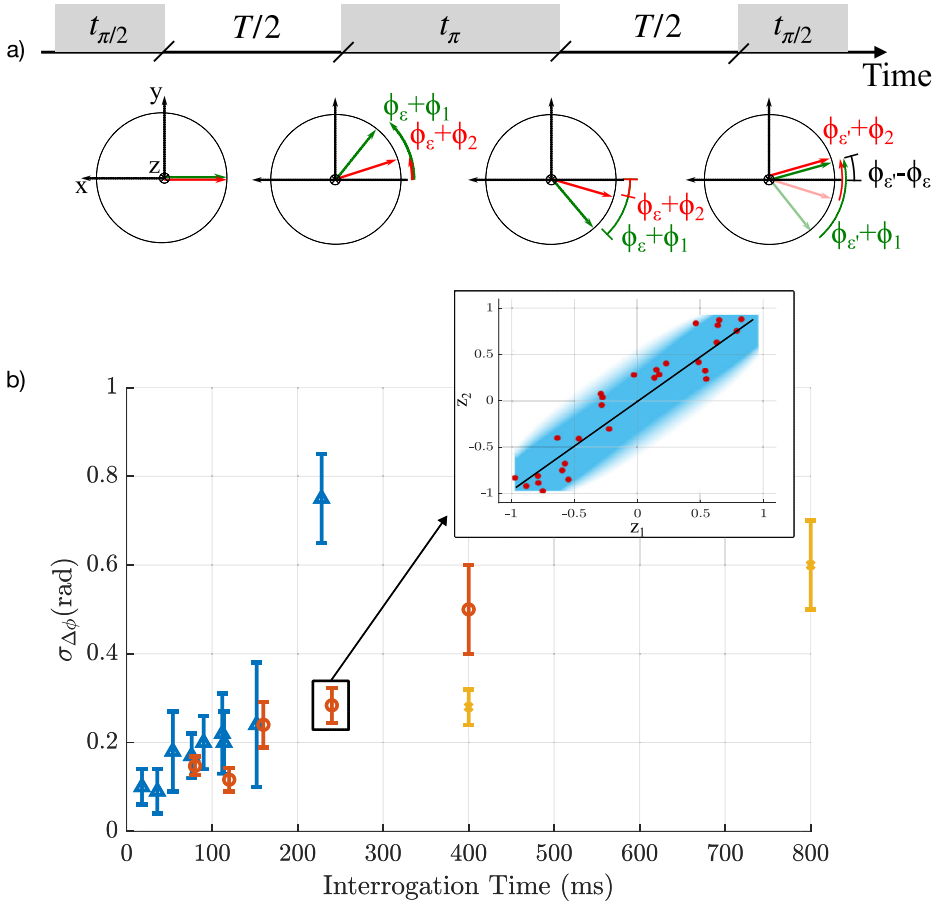

Fig. 5 | Gradiometer with spin-echo. a Evolution of the Bloch vectors of two interferometers during the spin-echo sequence. After the first beam-splitter, the arrows point along the -*x* direction. During the first *T*/2 time interval the two vectors are rotated by a DC random phase $\phi_{1,2}$ in addition to a common time varying random phase ϕ_ε. After a π pulse the vectors are mirrored with respect to the *x* axis. During the second *T*/2 time interval the random time varying common noise is indicated as $\phi_{\varepsilon'}$. At the end of the sequence, the rotations due to uncorrelated DC random noise is canceled and perfect correlation between the two vectors is achieved. **b** $\sigma_{\Delta\phi}$ of the gradiometer (blue points) and of the spin echo (red points) as a function of *T* at *B* = 350.45(6) Gauss. Yellow points are the spin-echo data taken at *B* = 350.48(1) Gauss. The error bars represent the standard deviation of the mean value computed with the Bootstrap method. The inset shows an example of output measurements showing the correlations between z_1 and z_2 data. The blue shaded region represents 90% confidence area of the fit.

provided by an intense 100 W IPG laser to perform the final evaporative cooling stage to achieve condensation[50]. Once a quantum degenerate gas is produced, this second laser is switched off in 300 ms while, after a time τ, the intensity of the BNSL with a spacing of 10 μm is ramped up. By changing the value of τ we can control the number of DWs populated. We can achieve a maximum number of 8 DWs with ≈2 × 10^3 atoms each. The three optical lattice lasers are frequency locked to the same optical cavity (see Supplemental Material). In this way cavity length drifts, to the first order, cause only spatial translation of the DWs array.

Theoretical modeling

The single interferometer can be described within a standard two-mode approximation of the many-body order parameter: $\Psi^\dagger(\boldsymbol{r}) = \psi_L(\boldsymbol{r})\hat{c}_L^\dagger + \psi_R(\boldsymbol{r})\hat{c}_R^\dagger$, where $\psi_{L,R}(\boldsymbol{r})$ are the wave function localized in the left and right well, respectively, and $\hat{c}_{L,R}^\dagger$ ($\hat{c}_{L,R}$) are bosonic mode creation (annihilation) operators, see e.g., ref. 40 for details. The mode wave functions are computed as $\psi_{L,R}(\boldsymbol{r}) = [\psi_{gs}(\boldsymbol{r}) \pm \psi_{ex}(\boldsymbol{r})]/\sqrt{2}$, where $\psi_{gs}(\boldsymbol{r})$ are the ground and first excited states of the non-interacting gas of energy E_{gs} and E_{ex}, respectively. We write the interaction potential as $U(\boldsymbol{r}-\boldsymbol{r}') = g\delta(\boldsymbol{r}-\boldsymbol{r}') + C_{dd}U_{dd}(\boldsymbol{r}-\boldsymbol{r}')$, where the first term accounts for elastic particle-particle interaction, with $g = 4\pi\hbar^2 a/m$, a being the s-wave scattering length that can be tuned by the magnetic field B, and the second term describe dipolar interaction $U_{dd}(\boldsymbol{r}-\boldsymbol{r}') = \frac{1}{4\pi}\frac{1-3\cos\theta}{|\boldsymbol{r}-\boldsymbol{r}'|^3}$. By neglecting the dipolar interaction between nearby wells of the BNSL, we write the interaction contribution to the full Hamiltonian, $H_{int} = \frac{1}{2}\int d\boldsymbol{r}\int d\boldsymbol{r}'\,\Psi^\dagger(\boldsymbol{r})\Psi^\dagger(\boldsymbol{r}')U(\boldsymbol{r}-\boldsymbol{r}')\Psi(\boldsymbol{r})\Psi(\boldsymbol{r}') = (\chi_{el}+\chi_{dip})J_z^2$, where $J_z = (\hat{c}_L^\dagger\hat{c}_L^\dagger - \hat{c}_R^\dagger\hat{c}_R^\dagger)/2$. For the parameters of our experiments, we estimate $\chi_{el} = 1.4464\frac{a}{x_0}\sqrt{\omega_y\omega_z} = 0.072\frac{a}{a_0}\,\mathrm{sec}^{-1}$, where $x_0 = 1\,\mu$m is the length unit in the code, a_0 is the Bohr radius ($a_0/x_0 = 5.3\times10^{-5}$), and $\chi_{dd} = -0.01\frac{C_{dd}}{\hbar x_0^3} = 0.01\,\mathrm{sec}^{-1}$. To summarize:

$$\hat{H}_{\mathrm{int}} = \hbar\times(0.072\frac{a}{a_0} - 0.01)\mathrm{Hz}\hat{J}_z^2. \tag{3}$$

It implies that the interaction within each double well of the superlattice potential can be exactly canceled when $\frac{a}{a_0} = 0.139$.

Multiparameter maximum likelihood estimation

We consider the set of *m* joint measurement results $\boldsymbol{z}_1 \equiv \{z_1^{(1)},\ldots,z_1^{(m)}\}$ and $\boldsymbol{z}_2 \equiv \{z_2^{(1)},\ldots,z_2^{(m)}\}$ obtained for the two interferometers and introduce the rescaled variable $\tilde{z}_j^{(k)} = (z_j^{(k)} - C_j)/V_j$. We assume that the output signal of each interferometer depends sinusoidally on the phase shift, with constant visibility V_j and offset C_j. The offset is estimated as $C_j = \sum_{k=1}^m z_j^{(k)}$ and, for our sets of data, where $m \approx 30$, we find $C_j \approx 0$ (see

e.g., caption of Fig. 3). The visibility is estimated as $V_j = \max_k |z_j^{(k)} - C_j|$. The phase difference $\Delta\phi$ and the uncorrelated noise $\sigma_{\Delta\phi}$ are estimated jointly, as the values that maximize the likelihood function $P(\tilde{z}_1, \tilde{z}_2|\Delta\phi, \sigma_{\Delta\phi}) = \prod_{k=1}^{m} P(\tilde{z}_1^{(k)}, \tilde{z}_2^{(k)}|\Delta\phi, \sigma_{\Delta\phi})$. A semi-analytical expression for $P(\tilde{z}_1, \tilde{z}_2|\Delta\phi, \sigma_{\Delta\phi})$ is obtained by assuming that the uncorrelated noise has a Gaussian distribution of width $\sigma_{\Delta\phi}$, giving

$$P(\tilde{z}_1, \tilde{z}_2|\Delta\phi, \sigma_{\Delta\phi}) = \frac{1}{(2\pi)^{3/2}\sigma_{\Delta\phi}\sqrt{1-\tilde{z}_1^2}\sqrt{1-\tilde{z}_2^2}} \left(\sum_{k=0,1} e^{-\frac{[\theta+(-1)^k(\sin^{-1}(\tilde{z}_1)-\sin^{-1}(\tilde{z}_2))]^2}{2\sigma_{\Delta\phi}^2}} + e^{-\frac{[\theta+(-1)^k(\sin^{-1}(\tilde{z}_1)+\sin^{-1}(\tilde{z}_2)-\pi)]^2}{2\sigma_{\Delta\phi}^2}} \right). \quad (4)$$

Further details about the multiparameter maximum likelihood method are reported in ref. 55. To associate error bars to the estimated values $\Delta\phi^{\text{est}}$ and $\sigma_{\Delta\phi}^{\text{est}}$ we use a Bootstrap method: we generate a large number of data z_1 and z_2 sampled according to $P(\tilde{z}_1, \tilde{z}_2|\Delta\phi^{\text{est}}, \sigma_{\Delta\phi}^{\text{est}})$. Data are divided into samples of m values. For every sample we obtain new estimated values of $\Delta\phi$ and $\sigma_{\Delta\phi}$. Finally, mean square fluctuations of the estimated values are computed.

Data availability

The data that support the findings of this study have been deposited in ref. 75.

References

1. Ketterle, W. Nobel lecture: When atoms behave as waves: Bose–Einstein condensation and the atom laser. *Rev. Mod. Phys.* **74**, 1131–1151 (2002).
2. Cornell, E. A. & Wieman, C. E. Nobel lecture: Bose–Einstein condensation in a dilute gas, the first 70 years and some recent experiments. *Rev. Mod. Phys.* **74**, 875–893 (2002).
3. Andrews, M. R. et al. Observation of interference between two Bose–Einstein condensates. *Science* **275**, 637–641 (1997).
4. Leggett, A. J. Bose–Einstein condensation in the alkali gases: Some fundamental concepts. *Rev. Mod. Phys.* **73**, 307–356 (2001).
5. Gross, C. & Bloch, I. Quantum simulations with ultracold atoms in optical lattices. *Science* **357**, 995–1001 (2017).
6. Pezzè, L., Smerzi, A., Oberthaler, M. K., Schmied, R. & Treutlein, P. Quantum metrology with non-classical states of atomic ensembles. *Rev. Mod. Phys.* **90**, 035005 (2018).
7. Amico, L. et al. Colloquium: atomtronic circuits: from many-body physics to quantum technologies. *Rev. Mod. Phys.* **94**, 041001 (2022).
8. Mewes, M.-O. et al. Output coupler for Bose–Einstein condensed atoms. *Phys. Rev. Lett.* **78**, 582–585 (1997).
9. Bloch, I., Häensch, T. W. & Esslinger, T. Atom laser with a cw output coupler. *Phys. Rev. Lett.* **82**, 3008–3011 (1998).
10. Cronin, A. D., Schmiedmayer, J. & Pritchard, D. E. Optics and interferometry with atoms and molecules. *Rev. Mod. Phys.* **81**, 1051–1129 (2009).
11. Herbst, A. et al. Matter-wave collimation to picokelvin energies with scattering length and potential shape control. *Commun. Phys.* **7**, 132 (2024).
12. Kovachy, T. et al. Quantum superposition at the half-metre scale. *Nature* **528**, 530–533 (2015).
13. Abe, M. et al. Matter-wave atomic gradiometer interferometric sensor (MAGIS-100). *Quantum Sci. Technol.* **6**, 044003 (2021).
14. Müntinga, H. et al. Interferometry with Bose–Einstein condensates in microgravity. *Phys. Rev. Lett.* **110**, 093602 (2013).
15. Condon, G. et al. All-optical Bose–Einstein condensates in microgravity. *Phys. Rev. Lett.* **123**, 240402 (2019).
16. Deppner, C. et al. Collective-mode enhanced matter-wave optics. *Phys. Rev. Lett.* **127**, 100401 (2021).
17. Beaufils, Q. et al. Cold-atom sources for the matter-wave laser interferometric gravitation antenna (MIGA). *Sci. Rep.* **12**, 19000 (2022).
18. Zhan, M.-S. et al. ZAIGA: Zhaoshan long-baseline atom interferometer gravitation antenna. *Int. J. Mod. Phys. D.* **29**, 1940005 (2020).
19. Aveline, D. et al. Observation of Bose–Einstein condensates in an earth-orbiting research lab. *Nature* **582**, 193–198 (2020).
20. Ferrari, G., Poli, N., Sorrentino, F. & Tino, G. M. Long-lived Bloch oscillations with bosonic Sr atoms and application to gravity measurement at the micrometer scale. *Phys. Rev. Lett.* **97**, 060402 (2006).
21. Charrière, R., Cadoret, M., Zahzam, N., Bidel, Y. & Bresson, A. Local gravity measurement with the combination of atom interferometry and Bloch oscillations. *Phys. Rev. A* **85**, 013639 (2012).
22. Hilico, A., Solaro, C., Zhou, M.-K., Lopez, M. & Pereira dos Santos, F. Contrast decay in a trapped-atom interferometer. *Phys. Rev. A* **91**, 053616 (2015).
23. Panda, C. D. et al. Coherence limits in lattice atom interferometry at the one-minute scale. *Nat. Phys.* **20**, 1234–1239 (2024).
24. Böhi, P. et al. Coherent manipulation of Bose–Einstein condensates with state-dependent microwave potentials on an atom chip. *Nat. Phys.* **5**, 592–597 (2009).
25. Pandey, S. et al. Hypersonic Bose–Einstein condensates in accelerator rings. *Nature* **570**, 205–209 (2019).
26. Moan, E. R. et al. Quantum rotation sensing with dual Sagnac interferometers in an atom-optical waveguide. *Phys. Rev. Lett.* **124**, 120403 (2020).
27. Pandey, S., Krzyzanowska, K. & Boshier, M. Multi-loop and multi-axis atomtronic Sagnac interferometry. *arXiv* https://doi.org/10.48550/arXiv.2504.20345 (2025).
28. Chai, X. et al. Continuously trapped matter-wave interferometry in magic Floquet–Bloch band structures. *Nat. Commun.* https://doi.org/10.1038/s41467-026-69299-y (2026).
29. Shin, Y. et al. Atom interferometry with Bose–Einstein condensates in a double-well potential. *Phys. Rev. Lett.* **92**, 050405 (2004).
30. Schumm, T. et al. Matter-wave interferometry in a double well on an atom chip. *Nat. Phys.* **1**, 57–62 (2005).
31. Jo, G.-B. et al. Phase-sensitive recombination of two Bose–Einstein condensates on an atom chip. *Phys. Rev. Lett.* **98**, 180401 (2007).
32. Maussang, K. et al. Enhanced and reduced atom number fluctuations in a BEC splitter. *Phys. Rev. Lett.* **105**, 080403 (2010).
33. Albiez, M. et al. Direct observation of tunneling and nonlinear self-trapping in a single bosonic Josephson junction. *Phys. Rev. Lett.* **95**, 010402 (2005).
34. Levy, S., Lahoud, E., Shomroni, I. & Steinhauer, J. The a.c. and d.c. Josephson effects in a Bose–Einstein condensate. *Nature* **449**, 579–583 (2007).
35. Spagnolli, G. et al. Crossing over from attractive to repulsive interactions in a tunneling bosonic Josephson junction. *Phys. Rev. Lett.* **118**, 230403 (2017).
36. Berrada, T. et al. Integrated Mach–Zehnder interferometer for Bose–Einstein condensates. *Nat. Commun.* **4**, 2077 (2013).
37. Lewenstein, M. & You, L. Quantum phase diffusion of a Bose–Einstein condensate. *Phys. Rev. Lett.* **77**, 3489–3493 (1996).
38. Javanainen, J. & Wilkens, M. Phase and phase diffusion of a split Bose–Einstein condensate. *Phys. Rev. Lett.* **78**, 4675–4678 (1997).
39. Berrada, T. et al. Matter-wave recombiners for trapped Bose–Einstein condensates. *Phys. Rev. A* **93**, 063620 (2016).
40. Pezzé, L., Smerzi, A., Berman, G. P., Bishop, A. R. & Collins, L. A. Nonlinear beam splitter in Bose–Einstein-condensate interferometers. *Phys. Rev. A* **74**, 033610 (2006).

41. Estève, J., Gross, C., Weller, A., Giovanazzi, S. & Oberthaler, M. K. Squeezing and entanglement in a Bose–Einstein condensate. *Nature* **455**, 1216–1219 (2008).
42. Gustavsson, M. et al. Control of interaction-induced dephasing of Bloch oscillations. *Phys. Rev. Lett.* **100**, 080404 (2008).
43. Fattori, M. et al. Atom interferometry with a weakly interacting Bose–Einstein condensate. *Phys. Rev. Lett.* **100**, 080405 (2008).
44. Balestri, D. *Incremento della coerenza in un interferometro con rumore mediante atomi interagenti*. Master's thesis, Università di Firenze (2015).
45. Burton, W. C. et al. Coherence times of Bose–Einstein condensates beyond the shot-noise limit via superfluid shielding. *Phys. Rev. Lett.* **117**, 275301 (2016).
46. Petrucciani, T. et al. Long-wavelength optical lattices from optical beatnotes: theory and applications. *Phys. Rev. A* **112**, 043323 (2025).
47. Snadden, M. J., McGuirk, J. M., Bouyer, P., Haritos, K. G. & Kasevich, M. A. Measurement of the Earth's gravity gradient with an atom interferometer-based gravity gradiometer. *Phys. Rev. Lett.* **81**, 971–974 (1998).
48. Hahn, E. L. Spin echoes. *Phys. Rev.* **80**, 580–594 (1950).
49. D'Errico, C. et al. Feshbach resonances in ultracold ^{39}K. *N. J. Phys.* **9**, 223 (2007).
50. Landini, M. et al. Direct evaporative cooling of ^{39}K atoms to Bose–Einstein condensation. *Phys. Rev. A* **86**, 033421 (2012).
51. Masi, L. et al. Spatial Bloch oscillations of a quantum gas in a "beat-note" superlattice. *Phys. Rev. Lett.* **127**, 020601 (2021).
52. Foster, G. T., Fixler, J. B., McGuirk, J. M. & Kasevich, M. A. Method of phase extraction between coupled atom interferometers using ellipse-specific fitting. *Opt. Lett.* **27**, 951–953 (2002).
53. Fixler, J. B., Foster, G. T., McGuirk, J. M. & Kasevich, M. A. Atom interferometer measurement of the Newtonian constant of gravity. *Science* **315**, 74–77 (2007).
54. Rosi, G., Sorrentino, F., Cacciapuoti, L., Prevedelli, M. & Tino, G. M. Precision measurement of the Newtonian gravitational constant using cold atoms. *Nature* **510**, 518–521 (2014).
55. Pezzè, L. et al. Joint estimation of phase and uncorrelated dephasing in a differential quantum interferometer. *arXiv* https://doi.org/10.48550/arXiv.2503.18166 (2025).
56. Fattori, M. et al. Magnetic dipolar interaction in a Bose–Einstein condensate atomic interferometer. *Phys. Rev. Lett.* **101**, 190405 (2008).
57. Andersen, M. F., Kaplan, A. & Davidson, N. Echo spectroscopy and quantum stability of trapped atoms. *Phys. Rev. Lett.* **90**, 023001 (2003).
58. Solaro, C. et al. Competition between spin echo and spin self-rephasing in a trapped atom interferometer. *Phys. Rev. Lett.* **117**, 163003 (2016).
59. Jo, G.-B. et al. Long phase coherence time and number squeezing of two Bose–Einstein condensates on an atom chip. *Phys. Rev. Lett.* **98**, 030407 (2007).
60. Obrecht, J. M. et al. Measurement of the temperature dependence of the Casimir–Polder force. *Phys. Rev. Lett.* **98**, 063201 (2007).
61. Carusotto, I., Pitaevskii, L., Stringari, S., Modugno, G. & Inguscio, M. Sensitive measurement of forces at the micron scale using Bloch oscillations of ultracold atoms. *Phys. Rev. Lett.* **95**, 093202 (2005).
62. Sorrentino, F. et al. Quantum sensor for atom–surface interactions below 10 μm. *Phys. Rev. A* **79**, 013409 (2009).
63. Balland, Y., Absil, L. & Pereira dos Santos, F. Quectonewton local force sensor. *Phys. Rev. Lett.* **133**, 113403 (2024).
64. Maiwöger, M. et al. Observation of light-induced dipole–dipole forces in ultracold atomic gases. *Phys. Rev. X* **12**, 031018 (2022).
65. Baroni, C., Gori, G., Chiofalo, M. L. & Trombettoni, A. Effect of inter-well interactions on non-linear beam splitters for matter-wave interferometers. *Condens. Matter* **5**, 31 (2020).
66. Mestrom, P. M. A., Colussi, V. E., Secker, T., Groeneveld, G. P. & Kokkelmans, S. J. van der Waals universality near a quantum tricritical point. *Phys. Rev. Lett.* **124**, 143401 (2020).
67. Pezzè, L., Collins, L. A., Smerzi, A., Berman, G. P. & Bishop, A. R. Sub-shot-noise phase sensitivity with a Bose–Einstein condensate Mach–Zehnder interferometer. *Phys. Rev. A* **72**, 043612 (2005).
68. Sinatra, A. Spin-squeezed states for metrology. *Appl. Phys. Lett.* **120**, 120501 (2022).
69. Kitagawa, M. & Ueda, M. Squeezed spin states. *Phys. Rev. A* **47**, 5138–5143 (1993).
70. Landini, M., Fattori, M., Pezzè, L. & Smerzi, A. Phase-noise protection in quantum-enhanced differential interferometry. *N. J. Phys.* **16**, 113074 (2014).
71. Corgier, R., Malitesta, M., Smerzi, A. & Pezzè, L. Quantum-enhanced differential atom interferometers and clocks with spin-squeezing swapping. *Quantum* **7**, 965 (2023).
72. Eckner, W. J. et al. Realizing spin squeezing with Rydberg interactions in an optical clock. *Nature* **621**, 734–739 (2023).
73. Jekeli, C. Navigation error analysis of atom interferometer inertial sensor. *Navigation* **52**, 1 (2005).
74. Bongs, K. et al. Taking atom interferometric quantum sensors from the laboratory to real-world applications. *Nat. Rev. Phys.* **1**, 731–739 (2019).
75. Petrucciani, T. et al. Mach–Zehnder atom interferometry with non-interacting trapped Bose–Einstein condensates. *Zenodo* https://doi.org/10.5281/zenodo.18097891 (2026).

Acknowledgements

We acknowledge financial support by the project SQUEIS of the QuantERA ERA-NET Cofund in Quantum Technologies (Grant Agreement No. 731473 and 101017733) implemented within the European Unions Horizon 2020 Program. We also thank the financial support of the Italian Ministry of Universities and Research under the PRIN2022 project "Quantum sensing and precision measurements with non-classical states". Finally, the project has been co-funded by the European Union—Next Generation EU under the PNRR MUR project PE0000023-NQSTI and under the I-PHOQS 'Integrated Infrastructure Initiative in Photonic and Quantum Sciences'.

Author contributions

T.P., A.Sa., and C.M. performed the experimental measurements; L.P. developed the theoretical model and performed the numerical simulations; M.F. supervised the experimental work; all authors contributed to the interpretation of the results and the writing of the paper.

Competing interests

The authors declare no competing interests.

Additional information

Supplementary information The online version contains supplementary material available at https://doi.org/10.1038/s41467-026-69692-7.

Correspondence and requests for materials should be addressed to L. Pezzè or M. Fattori.

Peer review information *Nature Communications* thanks the anonymous reviewer(s) for their contribution to the peer review of this work. A peer review file is available.